Journal of Advanced Joining Processes 9 (2024) 100218

Contents lists available at ScienceDirect

Journal of Advanced Joining Processes

journal homepage: www.sciencedirect.com/journal/journal-of-advanced-joining-processes

A sequential modelling approach to determine process capability space during laser welding of high-strength Aluminium alloys

Anand Mohan [a,*], Qamar Hayat [a], Soumitra Kumar Dinda [b], Venkat Vivek Pamarthi [a], Pasquale Franciosa [a], Dariusz Ceglarek [a], Michael Auinger [a]

[a] WMG, The University of Warwick, Coventry, CV4 7AL, United Kingdom
[b] Metallurgical and Materials Engineering, National Institute of Technology, Rourkela, India

ARTICLE INFO

Keywords:
Laser welding
High strength Aluminium
Process capability space
Beam oscillation
Numerical simulation

ABSTRACT

Remote laser welding (RLW) technology has become a prominent joining technology in automotive industries, offering high production throughput and cost-effectiveness. Recent advancements in RLW processes such as beam oscillation have led to an increased number of input process parameters, enabling precise control over the heat input to weld metallic materials. A critical necessity in laser welding entails selecting robust process parameters that satisfy all weld quality indicators or key performance indicators (KPIs) during two stages: production stage (often implemented as robotic welding); and repair/rework stage (implemented as cobotic/manual welding to identify process parameters for weld defects) as addressing these factors in both stages is necessary to satisfy near-zero-defect strategy for some e-mobility products.. This research presents a comprehensive methodology that encompasses the following key elements: (i) the development of physics-based simulations to establish the correlation between KPIs and process parameters; (ii) the integration of a sequential modelling approach that strikes a balance between accuracy and computation time to survey the parameter space; and (iii) development of the process capability space for the quick selection of robust process parameters.

Three physical phenomena are considered in the development of numerical models, which are (i) heat transfer, (ii) fluid flow and (iii) material diffusion to investigate the effect of process parameters on the weld thermal cycle, solidification parameters and solute intermixing layer during laser welding of dissimilar high-strength aluminium alloys. The governing physical phenomena are decoupled sequentially, and KPIs are estimated based on the governing phenomena. At each step, the process capability space is defined over the parameters space based on the constraints specific to the current physical phenomena. The process capability space is determined by the constraints based on the KPIs. The process capability space provides the initial combination of process parameter space during the early design stage, which satisfies all the KPIs, thus decreasing the number of experiments. The proposed methodology provides a unique capability to (i) simulate the effect of process variation as generated by the manufacturing process, (ii) model quality requirements with multiple and coupled quality requirements, and (iii) optimise process parameters under competing quality requirements.

Introduction

The automotive industry is aiming toward the reduction of body weight without hampering structural integrity. Davies et al. (Davies, 2003) suggested that the body-in-white and internal combustion engine (ICE) were the major contributors to the weight of the vehicle; therefore, body-in-white weight should be considered a critical design requirement for weight reduction. The development of lighter structures enables not only a decrease in fuel consumption but also allows the ability to use equivalent weight for cargo and passenger transportation. Aluminium alloys are usually the material of choice due to their abundance, low cost, recyclability, and corrosion resistance (Dinda et al., 2021; Goede et al., 2009; Sánchez Amaya et al., 2013). The new design solutions focus on using a higher proportion of aluminium alloys as a structural material or combining it with other automotive grades of aluminium alloys (Ramiarison et al., 2022). Sustainable manufacturing needs key enabling technologies that can help the welding industry understand and address environmental and economic challenges. This means

* Corresponding author.
E-mail address: anand.mohan@warwick.ac.uk (A. Mohan).

https://doi.org/10.1016/j.jajp.2024.100218

Available online 12 April 2024

producing products with near-zero defects, cheaper, better and faster. In essence, the laser welding processes need to be used at both, production stage (robotic welding) as well as repair/rework stage (cobotic/manual welding).

Remote Laser Welding (RLW) has emerged as a transformative technology in modern manufacturing, offering a long-distance focusing optic (hence "remote") to direct a high-powered laser beam. With the help of scanning mirrors, this beam is then precisely projected onto the workpiece, enabling welds in complex geometries and hard-to-reach areas. As an autogenous process, RLW eliminates the need for filler wire and shielding gas, further simplifying the process. Additionally, RLW offers reduced interference between the welding head and the part/fixture, allowing for "on-the-fly" welding and the creation of customized weld shapes to enhance joint strength on complex contours. RLW is one of the joining processes which can potentially meet the above-mentioned requirements as it offers a non-contact single-sided joining technology that allows high-speed welding for high-volume manufacturing (Ceglarek et al., 2015). It provides several advantages such as imposing heat in a very localised manner by modulating the power and location of the heat source which provides flexibility in terms of temperature, flow and concentration fields developed to weld new generations of lightweight alloys (Hagenlocher et al., 2018; Hagenlocher et al., 2019; EC Ozkat et al., 2017). It provides a high depth-to-width ratio, minimal distortion due to less heat input to the workpiece, high welding speed with remarkable processing efficiency and can be easily automated by embedding the laser optics on the robot and scanning mirror as an end-effector, for high productivity (Mahamood and Akinlabi, 2018; Salminen et al., 2010; Quintino et al., 2007). It creates a narrow fusion and heat-affected zone for less metallurgical changes to the workpiece. These advantages have accelerated the application of the RLW process for lightweight assembly in BEV manufacturing.

The selection of robust process parameters is important to avoid various unacceptable weld defects such as improper fusion, lack of penetration, and distortion. Currently, the quality of the weld is assured in four steps: (*i*) establishing optimum process parameters based on a trial and error approach; (*ii*) checking the variation (repeatability and reproducibility) and process capability of the selected process parameters for similar weld attributes and using the same parameters during the production phase; (*iii*) ensuring the required weld quality by performing various destructive and non-destructive weld characterisation techniques to estimate the KPIs; and (*iv*) conducting modification and refinement of the process parameters to satisfy all the KPIs.

There is an increase in the number of input process parameters due to the recent advancement in the RLW process for the better capability to weld different materials and joint configurations. A critical requirement for the manufacturing process is to select robust process parameters which produce parts within the defined specification limits. These specified limits are determined by the weld quality and other requirements of the downstream process. In general, weld quality refers to using the technological methods and actions that can guarantee quality by gathering and understanding the physical phenomenon occurring based on the process information and developing a quality control methodology to reduce the weld defects. This information can be obtained by offline inspection or by in-process monitoring (Guan et al., 2019; Chatterjee et al., 2006). The offline inspection is time and resource-expensive, reducing productivity and making it difficult to cope with the New Product Introduction (NPI) requirements. Furthermore, offline monitoring is used to develop a relationship between the process parameters and weld quality. In-line process monitoring is performed using sensors which convert surface radiation into electrical signals which are further converted to measurable variables. The data acquired by the sensors contain lots of noise, have a limited field of view and are unable to differentiate between various defects such as porosity, lack of penetration, microcracks, etc. (Chen and Gao, 2014; Speka et al., 2008). Both the use of traditional offline and in-line process monitoring have their own limitations and boundaries. The relationship between process parameters and weld quality is very critical, and in general, it is developed using statistical methods such as Response Surface Methodology (RSM). A large quantity of data is required to develop these relationships, which are obtained from the experiments and using sensors during experiments (Moradi and Ghoreishi, 2011; Gao et al., 2016, Zhang et al., 2016). Numerical simulation of laser welding can provide detailed information to obtain the relationship between the process parameters and the weld quality (Courtois et al., 2016; Pang et al., 2011; Rai et al., 2007; Otto et al., 2011). However, these models also provide details about the weld quality, which are either difficult or impossible to obtain by experiments such as thermal gradient, fluid flow, and weld thermal cycle (Hagenlocher et al., 2018; Hagenlocher et al., 2019; Chen et al., 2021). These outputs are important as they provide valuable insight into understanding the welding process such that the effects of process parameters on the weld quality can be understood.

Numerous researchers have utilised numerical models to generate processing maps, illustrating the relationship between weld quality and process parameters or derived parameters such as Peclet number (Pe_1), power density, and interaction time (Lankalapalli et al., 1996; Ion et al., 1992; Norouzian et al., 2023). These plots can be used to estimate the initial process parameters window based on the required weld quality. Mukherjee *et al.* (Mukherjee et al., 2017) explored the significance of heat transfer mechanisms, namely convection and conduction, in their study. The assessment of these mechanisms was achieved through the utilisation of the Peclet number (Pe_2). Ion et al. (Ion et al., 1992) developed a laser processing map between absorbed power density, interaction time and peak temperature and showed different regions of keyhole welding, cladding, cutting, melting and hardening. Lankalapalli et al. (Lankalapalli et al., 1996) developed the processing map between depth of penetration as a weld quality indicator and calculated the Peclet number for three different laser powers. In most of the literature depth of penetration was used as an indicator for the weld quality and derived parameters in place of actual welding process parameters for the development of laser processing map (Lankalapalli et al., 1996; Mannik and Brown, 1990, Swift- and Gick, 1973; Leong et al., 1997). Process capability space is a helpful for process parameters selection for various elements of assembly processes such as assembly fixture optimization (Franciosa et al., 2016) or even for assembled product design related with failures that occur when design parameters and process variables are within tolerance limits (in-specs) (Mannar and Ceglarek, 2010) or development of dimpling for laser welding of galvanized steel (EC Ozkat et al., 2017). Beam oscillation was not considered a parameter in any of the laser processing maps. Most of the laser processing map was based on the single input and single output (SISO) or multiple input single output scenario (MISO) whereas the RLW process is characterised by multiple inputs and multiple outputs (MIMO) scenarios (EC Ozkat et al., 2017). Therefore, a process capability space framework is proposed in this study to select robust process parameters based on the MIMO scenario.

High-strength aluminium alloys have high hot cracking susceptibility due to the rupture of the molten metal film at the grain boundaries during the solidification process (Coniglio et al., 2008; Weller et al., 2018, Easton et al., 2012; BJ, 1960). Current research efforts on Al-Si-Mg alloys involve extensive experimental investigations to mitigate hot cracking during welding. These efforts explore various approaches, including Al-Si cladding (Bamberg et al., 2024), pulsed beam welding techniques (Troise et al., 2024), and weld joint design optimization (Goyal and El-zein, 2020), with the ultimate goal of enhancing the mechanical properties of the welded structures. Welding of 5xxx and 6xxx high-strength aluminium alloys together is considered beneficial as it results in more acceptable chemistry and the weld chemistry is moved from the peak of the crack sensitivity curve (Norouzian et al., 2023; Chen et al., 2020). There are two possibilities to reduce susceptibility to hot cracking: (*i*) Optimisation of process parameters to influence solidification conditions to promote generating equiaxed grain structure in

the fusion zone; and (*ii*) Welding of dissimilar aluminium alloys and optimising the concentration of alloying elements by more mixing in the remote laser welding process. The formation of equiaxed grains and material mixing depends on the weld thermal cycle, convection due to fluid flow, solidification behaviour, and mass transport due to diffusion and convection. These weld attributes depend on the weld process parameters and proper selection of robust process parameters is critical and challenging to avoid weld defects. However, experiments are not sufficient to survey the parameters space as they are time and resource intensive. An alternative to the experimental investigation is a physics-driven model that numerically solves the governing physical phenomena to emulate the laser welding process. Even the survey of the whole parameters space by high fidelity numerical model is time intensive and not possible practically. The idea is to develop a process capability space framework based on a sequential modelling approach to reduce the computation time to quickly select robust process parameters. According to the reviewed literature, the research gap identified as: (*i*) characterisation of the laser welding process in the current literature is mainly based on a single input, single output or multiple input single output scenario, (*ii*) time intensive high-fidelity numerical model to survey the parameters space, and (*iii*) lack of a framework for quick assessment and selection of robust process parameters during the early design phase. The proposed approach of sequential modelling technique is to decrease the total computation time to determine the process capability space.

In the realm of zero-defect manufacturing requirements, for example for e-mobility products, simulations which enable determining process parameters (capability space) with desired process fallout rate (near-zero defects rate) are needed which are valid in two stages, i.e., (i) production stage which is often realized by using robotic laser welding process; and also for (ii) repair/rework stage which often cannot be done in an automatic mode (i.e., as robotic welding) and thus must be realized by using cobotic or even manual laser welding processes.

This paper underscores the pivotal role of simulation techniques in predicting and optimizing welding processes for both stages, i.e., production and repair/rework, thereby minimizing defects and enhancing overall product quality. Moreover, the integration of cobots into the weld repair and rework process is highlighted as a crucial advancement in Industry 5.0, enabling seamless collaboration between humans and machines for intricate tasks which cannot be fully automated due to time constraints or task complexity. The utilization of cobots not only streamlines the repair process but also ensures a safer working environment. In addition to optimizing process parameters during the robotic welding process, the development of process capability space offers invaluable insights into parameter selection for repair operations. By analyzing the capability space, manufacturers can discern optimal parameters tailored to specific repair scenarios, ensuring consistency and efficacy in the rework process. This comprehensive approach not only facilitates efficient robotic repair but also bolsters the adaptability of manufacturing systems to unforeseen challenges, thus contributing to the realization of zero-defect manufacturing objectives. Furthermore, in the context of Industry 5.0, the symbiotic relationship between humans and cobots in the repair process emerges as paramount. While cobots handle repetitive and hazardous tasks with precision, human oversight provides contextual understanding and problem-solving capabilities, fostering a collaborative environment where human expertise complements the capabilities of robotic systems, thereby ensuring robust and agile manufacturing processes. Furthermore, the paper delves into the significance of selecting optimal process parameters via process capability space analysis for robotic repair operations, elucidating how this approach enhances efficiency and consistency in weld rework tasks. Ultimately, by embracing simulation, process capability space analysis, and cobot-assisted repair, manufacturers can propel towards achieving the elusive goal of zero defects while aligning with the tenets of Industry 5.0.

Modelling strategy

Assumptions

A three-dimensional transient heat transfer and fluid flow model for laser welding has been developed, incorporating solute mixing arising from diffusion and convection. The model employs a hybrid volumetric heat source within a three-dimensional Cartesian coordinate system, where the positive *x*-axis represents the welding direction, the *y*-axis corresponds to the weld cross-section direction, and the *z*-axis is the direction of weld penetration. The motion of the heat source during beam oscillation is composed of two parts in the *x*-*y* plane, one is a circular motion and the other is a linear forward motion in the welding direction, resulting in an overall trajectory resembling a spiral. To enhance computational efficiency without significantly compromising numerical accuracy, the following assumptions have been made: (*i*) no gap between the two metal plates are considered, and resistance to heat, fluid, and mass transfer due to contact between the workpieces is neglected; (*ii*) Material properties are considered to be temperature-dependent; (*iii*) the fluid is modelled as Newtonian and incompressible, with Boussinesq's approximation accounting for density variations induced by temperature and concentration changes; (*iv*) the absorption coefficient is kept constant, presumed independent of temperature, and adjusted for model calibration based on weld profiles derived from experiments; (*v*) vapour and plasma flow is not simulated in the model, a Gaussian distributed volumetric heat source was considered which generates the heat inside the material such that fusion zone boundary lines are comparable to the experimental results (Farrokhi et al., 2019); and (*vi*) the mass and thermal diffusion coefficients of species are considered for the species in pure aluminium (*vii*) the simulation includes only Aluminium, Silicon, and Magnesium components, excluding other alloy elements due to their minimal concentration (*viii*) contributions to the temperature profile from exothermal reactions (e.g. oxidation) as originating from oxidation (i.e., exothermal reactions) and local effects of the shielding gas were not considered in this research work.

Governing equations

To determine the temperature distribution, velocity field and solute distribution, a coupled transient model was developed based on the solution of the equations of conservation of energy, mass and momentum and solute transport as given in Eqs. (1)–(4) (Atabaki et al., 2014; Geng et al., 2020; Wu et al., 2018; A Mohan et al., 2023).

Energy conservation

$$\rho C_P \frac{\partial T}{\partial t} + \rho C_P u.\nabla T = \nabla.(\lambda \nabla T) + Q_{laser} \tag{1}$$

Mass conservation

$$\nabla.(u) = 0 \tag{2}$$

Momentum conservation

$$\rho \frac{\partial (u)}{\partial t} = -\rho \nabla.(uu) - \nabla P + \nabla.\eta(\nabla u) + F \tag{3}$$

Solute transport equation

$$\frac{\partial (\rho C_i)}{\partial t} + u.(\nabla C) = \nabla.\left(D_i \nabla C_i + D_{Ti} \frac{\nabla T}{T}\right) + \rho g \beta_c (C - C_{ref}) \tag{4}$$

where ρ is the material density, c_p is the specific heat capacity of the material, T is the temperature of the workpiece, t is the time, k is the thermal conductivity of the material, Q_{laser} is the energy input of the laser heat source, u is the velocity of the fluid, P is the static pressure, η is the dynamic viscosity of the fluid, C_i is the concentration of species *i*, D_i is the mass diffusion coefficient for species i and D_{Ti} is the thermal

diffusion for species *i*, and *F* is the force term which is defined in Eq. (5). The first term on the left-hand side of the Eq. (4) represents the rate of change of the mass concentration of species *i* (C_i) with respect to time (t). It accounts for the temporal variation of the concentration. The second term on the left-hand side of Eq. (4) represents the convective flux of species *i* and (∇C) represents the concentration gradient. The dot product of these two quantities represents the flux of the species due to fluid convection. The first term on the right-hand side of Eq. (4) represents the diffusive flux of species *i*. This term accounts for the diffusive transport of the species driven by concentration and temperature gradients. The second term on the right-hand side of Eq. (4) represents the buoyancy effect, often referred to as "buoyancy-driven convection" or "buoyancy-driven diffusion". This term accounts for the movement of the species caused by density variations induced by temperature differences. Eq. (4) combines the effects of temporal changes in concentration, convective transport, diffusive transport driven by concentration and temperature gradients, and buoyancy-driven convection to describe the overall movement and transport of species *i* in a fluid. The first term in Eq. (5) is according to the Carman-Kozeny equation for flow through a porous media (Abderrazak et al., 2009) representing the frictional dissipation which ensures a smooth transition of velocity from zero to a large value in the mushy zone. The second term on the right-hand side of Eq. (5) accounts for natural convection.

$$F = C\left(-\frac{(1-f_l)^2}{f_l^3+B}\right)u + \rho g\beta\left(T-T_{melting}\right) \tag{5}$$

where *B* is a merely computational constant, a very small positive number to avoid division by zero is set at 0.001 and *C* is a mushy zone constant related to the morphology of the porous media which is a large number (a value of 1.6 x 10^4 was used in the present study) to force the velocity of the solid zone to be zero and represents mushy zone morphology, β is the coefficient of volume expansion, *g* is the acceleration due to gravity, $T_{melting}$ is the melting temperature which is average of solidus and liquidus temperature and f_l is the fraction of liquid which is defined in Eq. (6) where, T_{liq} and T_{sol} are liquidus and solidus temperature of the materials respectively .

$$f_l = \begin{cases} 1 & T > T_{liq} \\ \dfrac{T-T_{sol}}{T_{liq}-T_{sol}} & T_{sol} \le T \le T_{liq} \\ 0 & T < T_{sol} \end{cases} \tag{6}$$

The phase changes are considered to include temperature change due to latent heat by using the apparent heat capacity method which includes an additional term for latent heat as given in Eq. (7)

$$C_P = C_{P,solid}.(1-f_l) + C_{P,liquid}.f_l + L_{s\to l}\frac{\Delta f_l}{\Delta T}H_m \tag{7}$$

Where, $C_{p,solid}$ is the heat capacity of the solid phase, $C_{p,liquid}$ is the heat capacity of the liquid phase and H_m is the melting latent heat.

Heat source model

A hybrid heat source is adopted to simulate the heat input to the workpiece. The general trajectory of the moving heat source is given in Eq. (8) where $x_{(t)}$, $y_{(t)}$ and $z_{(t)}$ are time-dependent heat source spot coordinates, x_0, y_0 and z_0 mark the initial position of the heat source, *S* is the welding speed, *R* is the radius of oscillation, *t* is the time and *f* is the oscillation frequency. The term *St* gives the displacement in the welding direction, *(1-Rcos(2πft))* and *Rsin(2πft)* produce the circular rotation for the oscillation of the beam.

$$\left(x_{(t)},\ y_{(t)},\ z_{(t)}\right) = \begin{cases} (x_0 - St,\ y_0\ ,\ z_0) & \textit{No oscillation} \\ (x_0 + St - R(1-cos(2\pi ft)),\ \ y_0 + Rsin(2\pi ft),\ \ z_0) & \textit{Beam oscillation} \end{cases} \tag{8}$$

A modified Gaussian damped heat source and a double ellipsoid heat source are used to describe heat distribution. The Bremsstrahlung absorption is modelled by the double ellipsoid heat source (Slováček et al., 2005) and is described as follows:

$$Q_f(x,y,z,t) = \eta\frac{6\sqrt{3}f_f P_l}{a_f bc\pi\sqrt{\pi}}e^{-3\frac{\left(x-x_{(t)}\right)^2}{a_f{}^2}}e^{-3\frac{\left(y-y_{(t)}\right)^2}{b^2}}e^{-3\frac{\left(z-z_{(t)}\right)^2}{c^2}} \tag{9}$$

$$Q_f(x,y,z,t) = \eta\frac{6\sqrt{3}f_r P_l}{a_r bc\pi\sqrt{\pi}}e^{-3\frac{\left(x-x_{(t)}\right)^2}{a_r{}^2}}e^{-3\frac{\left(y-y_{(t)}\right)^2}{b^2}}e^{-3\frac{\left(z-z_{(t)}\right)^2}{c^2}} \tag{10}$$

where P_l is the power of the heat source beam, *r* is the heat source spot radius, a_r, a_f, *b*, and *c* are the heat source distribution parameters depending upon the shape of the weld pool obtained by measuring the rear (a_r), front (a_f), width (b), depth (c) of the half ellipsoids, Q_f *(x,y,z,t)* and Q_r *(x,y,z,t)* are the power densities in the front and rear quadrant of the double ellipsoid heat source. η is the absorption coefficient of the metal whose value is taken as 0.60 based on the previous studies (Sun et al., 2022; A Mohan et al., 2023). The Gaussian damped heat source is modified to account for the decay of the heat distribution through the thickness of the workpiece instead of specifying it to the depth of penetration. In general, the depth of penetration is provided as input in the model which is calculated experimentally or by interpolation using a surrogate model based on a few experiments. The experimental calculation will not serve the advantages of performing numerical simulations to predict the fusion zone dimensions. The modified Gaussian damped hybrid heat source eliminates the requirement of providing depth of penetration as an input and is defined as:

$$Q_{mgd}(x,y,z,t) = \eta\frac{6P_l}{\pi r^2 d(1-e^{-3})}\frac{mz+r}{md+2r}e^{-3\frac{\left(x-x_{(t)}\right)^2+\left(y-y_{(t)}\right)^2}{r^2}}e^{-3\frac{\left(z-z_{(t)}\right)^2}{d^2}} \tag{11}$$

Where *d* is the thickness of the material and *m* is the damping coefficient is selected to minimise the simulated errors which are taken 0.1 in this study. The effective heat absorbed by the hybrid Gaussian damped heat source and double ellipsoid combined is given by Eq. (12). f_3 and f_2 are the power distribution coefficient between the Gaussian damped and double ellipsoid heat source respectively which follows $f_1 + f_2 = 1$ and in this study, it is set as $f_2 = 0.6$.

$$Q_{laser}(x,y,z,t) = f_1\left(Q_r(x,y,z,t) + Q_f(x,y,z,t)\right) + f_2 Q_{mgd}(x,y,z,t) \tag{12}$$

Boundary conditions

The initial temperature of the workpiece is assumed to be maintained at room temperature (T_0). The energy absorbed by the workpiece is transferred by conduction, which further is partially lost due to contact with the ambient atmosphere and by radiation leading to cooling. The heat loss due to the contact with the ambient atmosphere and by radiation during welding is governed by Newton's law of cooling and the Stefan-Boltzmann relation (Shi et al., 2016) is defined as:

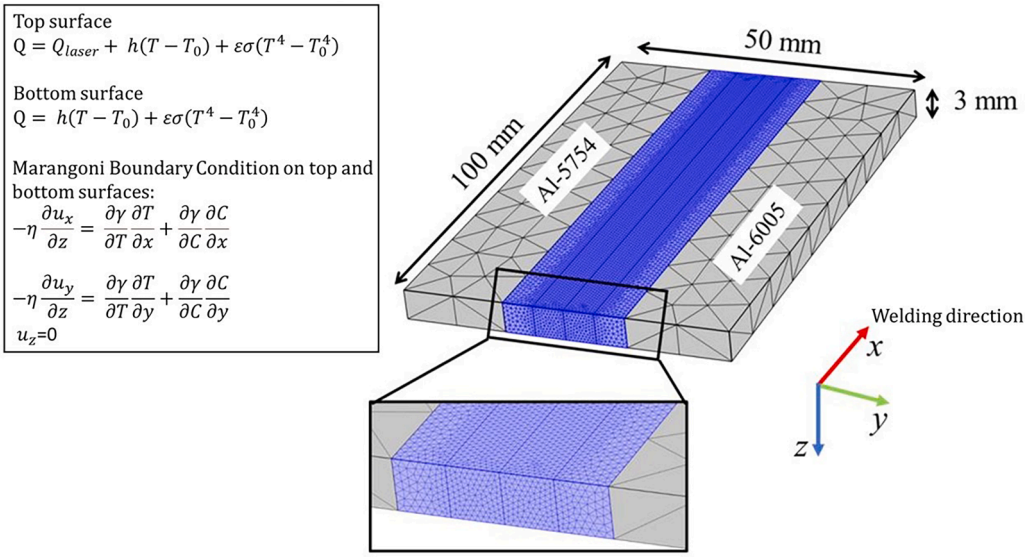

Fig. 1. Schematic illustration of geometry and finite element mesh distribution used for the simulations. Image has been reproduced and modified from [52] with permission.

$$-k\nabla T = h(T - T_0) + \varepsilon\sigma\left(T^4 - T_0^4\right) + Q_{vap} \tag{13}$$

where h is the surface heat transfer coefficient, ε is the emissivity of the material and σ is the Stefan-Boltzmann coefficient of radiation. The heat loss due to vaporisation $Q_{vap} = WL_v$ where W is the evaporation rate and L_v is the latent heat of vaporisation. The effect of surface tension gradient due to the variation in temperature and concentration on the top surface of the workpiece is given in Eq. (14)-(15) (Wu et al., 2018) and the velocity along the z-direction is zero.

$$-\eta\frac{\partial u_x}{\partial z} = \frac{\partial\gamma}{\partial T}\frac{\partial T}{\partial x} + \frac{\partial\gamma}{\partial C}\frac{\partial C}{\partial x} \tag{14}$$

$$-\eta\frac{\partial u_y}{\partial z} = \frac{\partial\gamma}{\partial T}\frac{\partial T}{\partial y} + \frac{\partial\gamma}{\partial C}\frac{\partial C}{\partial y} \tag{15}$$

Calculation domain and numerical implementation

In the current study, Al-6005 and Al-5754 alloys are joined in a butt joint configuration, employing a circular beam oscillation pattern without nominal gaps between the workpieces. The numerical model is executed using COMSOL 5.6 Multiphysics software, employing the finite element method for spatial discretization and the BDF method for time discretization. The simulation domain for a single plate measures 100 mm × 25 mm × 3 mm. Each plate is divided into three segments to enhance mesh distribution by transitioning from a fine mesh at the centre of the fusion zone to a coarser mesh towards the base metal, as depicted in Fig. 1. A mesh sensitivity analysis is conducted across the entire temperature and fluid velocity domains, and model outputs are computed after the model achieves quasi-steady state conditions in terms of temperature and fluid flow fields. A tetragonal mesh is used with a minimum mesh size of $r/8$ mm having a total number of mesh elements of 750,639 elements over the whole domain. To map the effect of oscillation of frequency, the time step is selected as $1/(4f)$ seconds. The thermophysical properties of AA-5754 and AA-6005 alloys are taken from (Behúlová et al., 2017; Guo et al., 2010) and the COMSOL materials library (COMSOL August 16, 2022). These properties are defined locally using a piecewise function and the data of the material properties is available from the room temperature to the vaporization temperature. In case of unavailability of material properties beyond a certain temperature near the boiling point, the values are taken as constant for the last known temperature. Just to note that the calibration

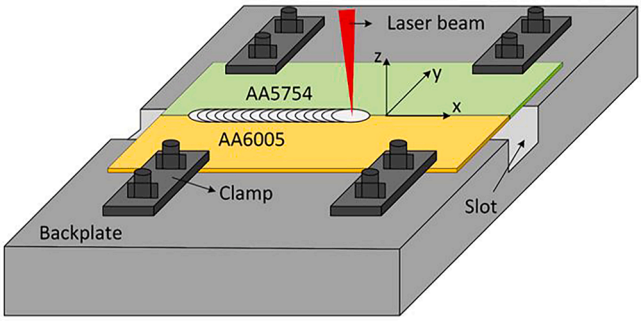

Fig. 2. Laser welding experimental schematics.

and validation of heat transfer, fluid flow and material mixing models are discussed in the author's previous work (A Mohan et al., 2023; A Mohan et al., 2023; A Mohan et al., 2022; A Mohan et al., 2022). The validity of the heat transfer model was established by comparing the simulated thermal cycles with experimentally obtained thermocouple data and weld widths for both non-oscillating and beam-oscillating conditions (A Mohan et al., 2022; A Mohan et al., 2022). The fluid flow model was validated through a two-pronged approach. Firstly, the model's predicted fusion zone shape and dimensions were compared with those measured via optical microscopy (A Mohan et al., 2023; A Mohan et al., 2022). Secondly, the model's estimates of the top surface weld pool morphology were compared with high-speed camera observations (A Mohan et al., 2023; A Mohan et al., 2023). Validation of the material mixing model was achieved by comparing the experimentally measured solute distribution, obtained using EDS line scans, with the simulated distribution (A Mohan et al., 2023). The close agreement between experimental and simulated results, with an average percentage error of only 4.95 %, demonstrates the effectiveness of the employed models.

Table 1
Chemical composition of Aluminium alloys in weight%.

Composition	Mg	Si	Mn	Cr	Cu	Fe	Al
AA-5754	2.6–3.6	0.6–0.9	≤ 0.5	≤ 0.3	≤ 0.1	–	Bal.
AA-6005	0.4–0.8	0.9–1.4	≤ 0.1	≤ 0.1	≤ 0.1	≤ 0.35	Bal.

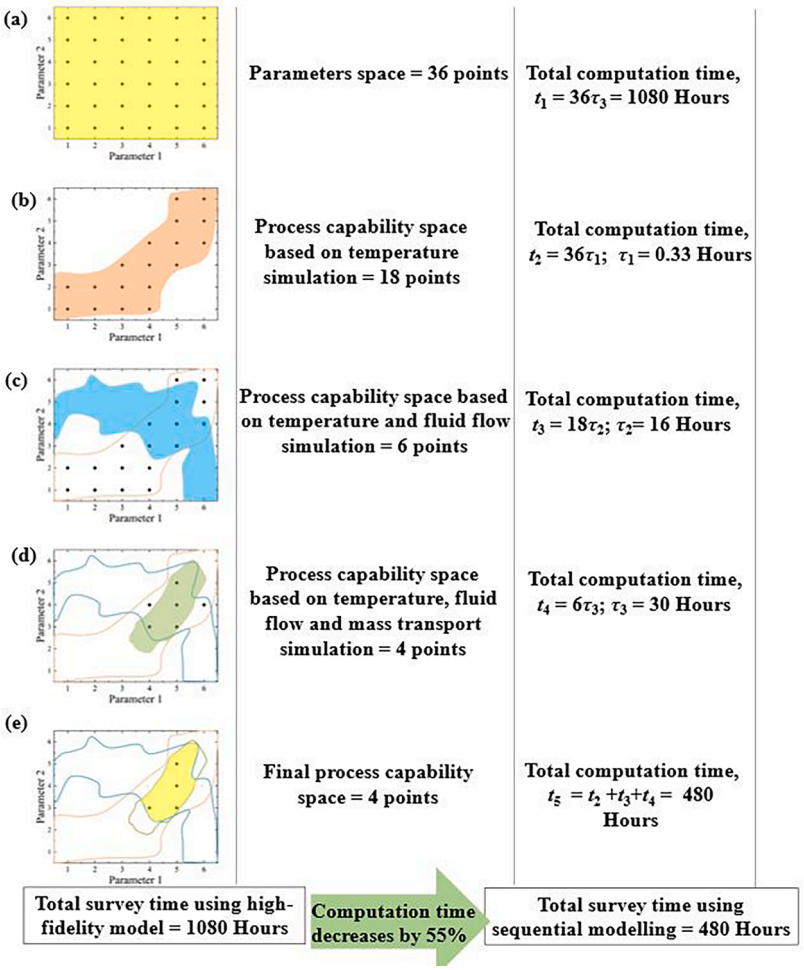

Fig. 3. Schematic illustration of the sequential modelling approach for complete parameters space search (a) two process parameters space, process capability space based on (b) temperature, (c) temperature and fluid flow, (d) temperature, fluid flow and mass transport simulation and (e) the final process capability space. .

Experimental setup

A Coherent ARM FL10000 laser system with 10 KW power capacity with a beam parameter product of 16 mm mrad with a core optical fibre of 100 μm diameter was used. The laser system coupled with the WeldMaster remote welding head (Precitec GmbH, Germany) and beam oscillation is generated by the motorised mirror and collimator integrated with the WeldMaster Scan&Track remote welding head. Only a core beam was used to carry out the experiments. The Guillotine cutter was used to machine the sheets into a coupon having dimensions 100 mm × 50 mm × 3 mm. Neither filler wire nor shielding gas was used throughout the experiments. Welding experiments are carried out in butt joint configurations and the incident beam is inclined at an angle of 4° with a focal offset of 13 mm. Fig. 2 provides a schematic representation of the experimental setup, detailing the joint configuration and the positioning of clamps. The chemical composition of the Al-6005 and Al-5754 alloys used in the experiments is presented in Table 1.

Just to note that all the experimental results for the laser welding of Al-5754 and Al6005 used for the calibration and validation of the numerical models and to define the Intermediate Performance Indicators (IPIs) are detailed discussed in previous work of the author (A Mohan et al., 2023; A Mohan et al., 2023; A Mohan et al., 2022; A Mohan et al., 2022).

Results and discussions

The flexibility of RLW increases the number of initial weld process parameters whose effect needs to be understood and the selection of robust parameters is challenging especially based on the current method of trial and error. The selection of robust welding process parameters (WPP) is critical to satisfying the weld quality requirements which depend on the requirements of the downstream processes such as weld strength, weld dimensions and shape. With the increasing number of input process parameters, it is impractical to survey the parameters space by experiments alone as it is time and resource intensive. Therefore, the development of a numerical model is essential to establish the relationship between the weld quality and process parameters for the selection of robust process parameters during the design phase with a minimum number of experiments. High-fidelity numerical models require large computational time to solve which makes it impractical to survey the whole parameters space for the selection of robust process parameters whereas low-fidelity numerical models are able to describe the most prominent physics at a reduced computation time and resources. Therefore, a sequential modelling approach is proposed to balance between high accuracy and computation time (i.e., high-fidelity models) and low computation resource requirements models (i.e., low-fidelity models). The main steps to survey the parameters space using a sequential modelling approach are: (i) first step is the development of a low-fidelity model based on one or two independent phenomena: (ii) defining IPIs/KPIs based on the physical phenomena with the allowable constraints to achieve the required weld quality; (iii) the WPPs within the allowable limits of IPIs/KPIs are selected and the region or space is defined as process capability space; (iv) in the low-fidelity model, next governing phenomena is added; (v) new IPIs and KPIs are defined based

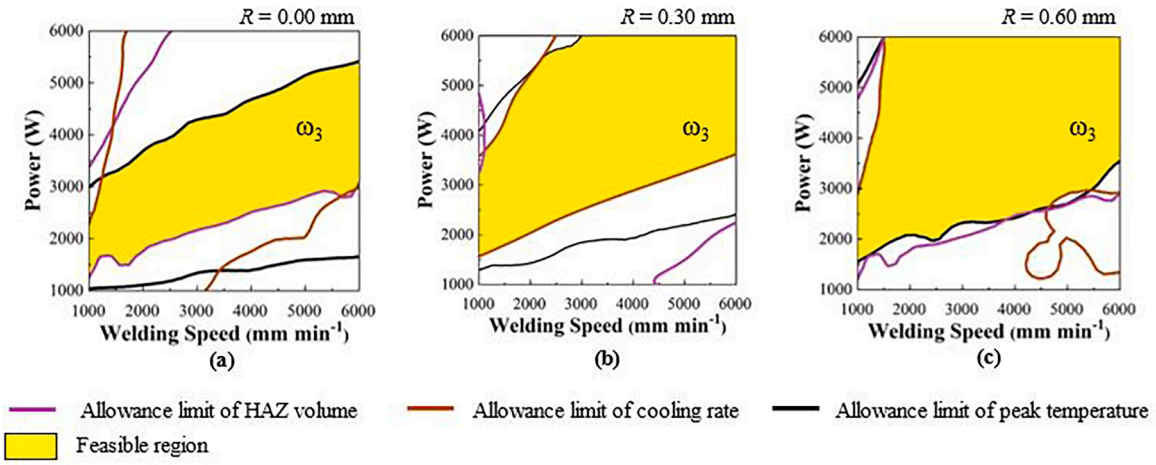

Fig. 4. shows the process capability space for three process parameters to show the 3D response surface as a stacked-up 2D contour map. The z-axis for the 3D response surface is the radius of oscillation which is varied at (a) $R = 0$ mm, (b) $R = 0.30$ mm, and (c) $R = 0.60$ mm. Image has been reproduced and modified from (A Mohan et al., 2022) with permission.

on the new physical phenomena and constraints are defined based on the required weld quality; (vi) the process capability space defined in the step (iii) is used instead of complete parameters space to define the new process capability space due to the addition of newly added phenomena. In this sequential modelling approach, a low-fidelity model based on a particular physical phenomenon such as heat transfer is developed to mirror the flow of heat but leave out all other physical phenomena such as mechanical deformation, fluid flow, and element transport. Relevant KPIs/IPIs are determined which is described by this low-fidelity model and the whole parameters space is surveyed. Based on the constraints on the KPIs/IPIs depending on the weld quality, the allowable WPPs are selected and these WPPs are feasible and can be selected for the welding such that they will maintain the weld quality which is assessed by the respective IPIs/KPIs. The combination of all possible WPPs within the allowable limits of the IPIs/KPIs is defined as the process capability space. In the next step, another governing physical phenomenon is added to the low-fidelity model which describes new KPIs/IPIs. However, in this step, only the determining process capability space of the previous step is surveyed. Just to note here that before the development of process capability space it must be tested if the newly added phenomena have an impact on the output under consideration. Again, new constraints are added to the new KPIs/IPIs and a more refined region on the parameters space is developed. This decreases the computational time as at each step fewer points or smaller regions are required to be solved by the numerical model to survey the whole parameters space which is illustrated in Fig. 3. It presents the schematic illustration of the sequential modelling approach.

In Fig. 3 column one represents the parameters space (Fig. 3(a)) or process capability spaces (Fig. 3(b)-(e)), and the dotted points on these spaces represent the input parameter combinations for the numerical model to solve for, column two represents the number of simulations that need to be run to survey the parameter space and column three provides the computation time needed to solve to survey the respective space at each stage. It should be noted that the computation time mentioned is the average time taken to compute the numerical model to simulate the laser welding process based on the finite element method developed in this study. Three physics-driven phenomena are solved to survey the parameters space (Fig. 3(a)), which are heat transfer, fluid flow and material mixing (mass transport). High fidelity model is a combination of all three physics which takes 36 h (computation time as presented in this study) to compute a solution using a numerical model for each data point in the parameters space. Parameters space is defined as the area of the multidimensional combinations and interactions of process parameters (WPPs) and input variables that have been illustrated to assure quality (Courtois et al., 2016). It is a function or a relation between the critical WPPs and critical IPIs/KPIs. Fig. 3 shows that there is a decrease in computational time by more than 55 % to survey the parameters space using the sequential modelling approach.

The sequential modelling approach discussed above is used to develop the final process capability space for the laser welding of Al-5754 with Al-6005 alloys in butt joint configuration. The main welding parameters considered in this study are welding speed, laser power and radius of oscillation. Fig. 4 shows the process capability space based on the heat transfer model for different radius of oscillation. The detail development of process capability space based on heat transfer model was considered in previous work (A Mohan et al., 2022). Three IPIs are defined based on the heat transfer model which are peak temperature, cooling rate and HAZ volume. The shaded area in yellow represents the feasible region and any process parameters inside this region satisfy all the requirements. The final process capability space is the intersection of process capability space of individual IPI. The final process capability space includes all the feasible welding process parameters. the size of the process capability space increases and is applicable for broader process parameter ranges with an increasing radius of oscillation. This demonstrates the increase in flexibility of the laser welding process due to the application of beam oscillation.

In the previous study, it was found that the ratio of equiaxed grains area to fusion zone has a direct relation with the mechanical strength of the welds (A Mohan et al., 2023). Higher the ratio higher will be the mechanical strength. Also, during butt welding depth of penetration is an important factor affecting the weld strength as higher the depth of penetration higher will be the fusion between the two components. The two IPIs defined based on the heat transfer and fluid flow model are penetration depth (D_p) and the ratio of the width of an equiaxed zone (FZ1) and fusion zone (FZ) (W_{eqx}) at the top surface of the workpiece. The ratio of the width of the equiaxed and fusion zone is representative of the percentage of the equiaxed grains formed in the fusion zone. In laser welding, G/R values suggest the formation of columnar and equiaxed grain in the fusion zone (Sun et al., 2022; A Mohan et al., 2023). The behaviour or criteria of transition of columnar grains into equiaxed grains have been well investigated in the literature (Hunt, 1984; Gäumann et al., 2001; Flood and Hunt, 1987), so only the final mathematical expression is discussed here, which describes the relationship between volume fraction of the equiaxed grains Φ, material-dependent and primary solidification parameters (Gäumann et al., 2001; Geng et al., 2020):

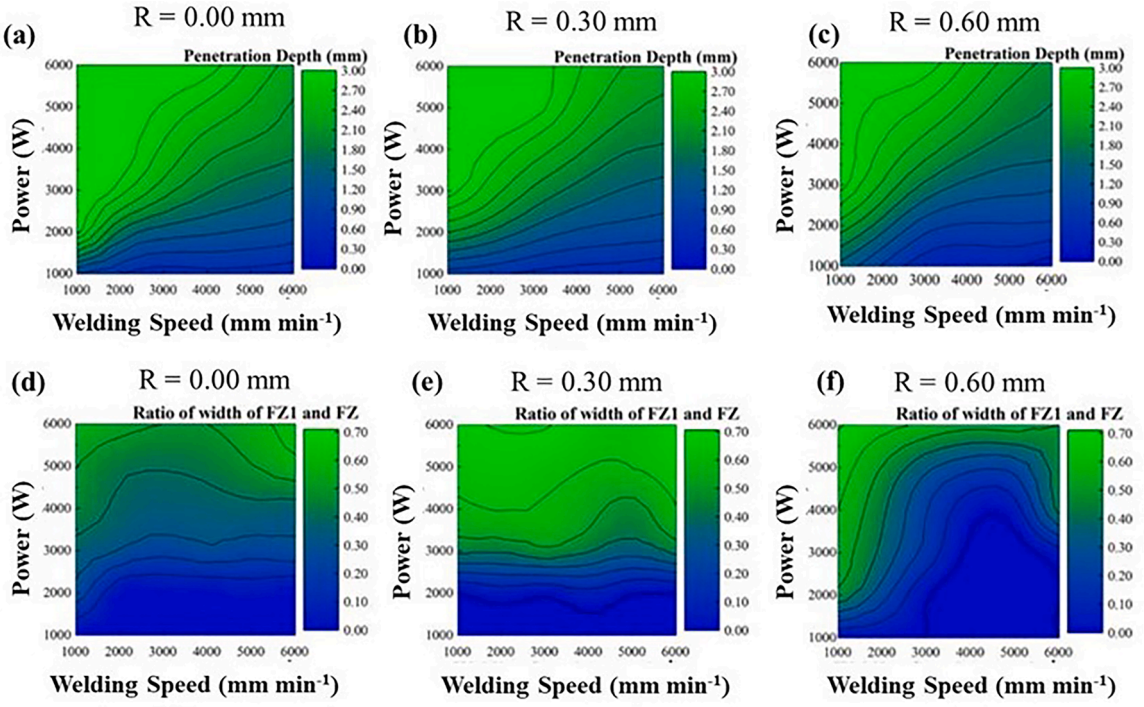

Fig. 5. Parametric contour maps for laser power vs welding speed with and without oscillation conditions at a constant frequency of oscillation of 200 Hz. (a-c) shows a contour map for penetration depth and (d-f) shows contour maps for the ratio of the width of the equiaxed zone (FZ1) and fusion zone (FZ).

$$\frac{G^n}{R} = a\left[\frac{1}{n+1}\left(\frac{-4}{3}\frac{\pi N_0}{ln(1-\Phi)}\right)^{\frac{1}{3}}\right]^n \tag{16}$$

$$\Delta T = (aV)^{1/n}, \tag{17}$$

where a and n are material-dependent properties for the constitutional tip undercooling for the growth of columnar and equiaxed dendritic growth as defined in Eq.(17). ΔT is the undercooling and V is the dendrite growth rate, which is approximated as the solidification rate, R. Hunt (Hunt, 1984) found that $\Phi > 0.49$ should be considered for the fully equiaxed growth. Greer (Vandyoussefi and Greer, 2002) proposed the value for the material dependent parameters as $n = 3$ and $a = 6.19\ K^3$ m/s and N_0 is fitted to the value of $2.77 \times 10^{13}\ m^{-3}$ for Al5xxx alloys. Geng et al. (Geng et al., 2020) provided the critical condition for fully equiaxed grain formation as $G^3/R < 1.66 \times 10^5\ K^3\ s/mm^4$. Based on this critical value for the equiaxed grain formation the width of the equiaxed grains was calculated from the numerical model. The parametric contour map for the penetration depth and width of the ratio of FZ1 and FZ is shown in Fig. 5 for no oscillation and beam oscillation conditions with $R = 0.3$ mm and $R = 0.6$ mm.

As expected, the penetration depth increases with an increase in power or decrease in welding speed for both with and without beam oscillation as shown in Fig. 5 (a-c). Also, for the same combinations of welding speed and power, the depth of the penetration decreases with beam oscillation due to the decrease in heat input per unit length. The ratio of the width of the equiaxed region and fusion zone increases with an increase in laser power due to a decrease in thermal gradient due to an increase in the temperature of the weld pool. As the thermal gradient decreases more regions of the fusion zone have equiaxed grain formation due to a decrease in G^3/R. At the constant depth of penetration, the W_{eqx} increases with the beam oscillation and even increases with an increase in the oscillation radius. This is due to an increase in solidification rate R with the beam oscillation and also a decrease in thermal gradient G which decreases the total value of G^3/R, so more regions of equiaxed grains will form.

Fig. 6 shows the process capability space for no oscillation welding based on the penetration depth and ratio of the width of the equiaxed zone and fusion zone. The upper limit for the D_p is through the thickness of the workpiece as in principle higher the penetration higher will be the strength in the case of butt-welding joint configuration. The lower limit of D_p is selected as 75 % of the thickness of the plate because below this range the interface at the bottom region of the fusion zone act as a stress raiser which hampers the mechanical strength of the joint. Based on the experimental results in the previous section the lower limit of W_{eqx} is selected as 0.45 and the upper limit is the highest possible value. A larger region of equiaxed grains, it generates more grain boundaries which hinder the crack propagation and improves the mechanical performance of the joints (Hagenlocher et al., 2018; Hagenlocher et al., 2019). ω_3 is the process capability space based on the weld thermal cycle model, ω_4 is the process capability space based on the penetration depth and ω_5 is the final process capability space based on the combined weld thermal cycle and fluid flow model. It should be noted that the ω_3 will have the same region even if the order of IPIs is changed. Also, for butt welding, the penetration depth is considered an important KPI but for simplicity, it is termed IPI in this study. The final process capability space (ω_5) from the combined weld thermal cycle and fluid flow model will be the initial region or in other words parameters space when the material mixing is included.

Fig. 7 shows the effect of beam oscillation on the process capability space. It can be also visualised as the stack up of 2D contour maps in the xy plane at a constant third process parameter. The process capability space will represent a plane in the 3D space which has been sectioned at a constant value of the third process parameter for better visualisation. The process capability space increases with the application of beam oscillation which suggests that the beam oscillation provides an extra degree of freedom to modify the weld thermal cycle, fluid flow and solidification behaviour of the weld.

Fig. 8 shows the simulated ratio of the width of the intermixing layer (IML) and the width of the fusion zone at the top surface of the workpiece for different combinations of welding speed and laser power for both with and without beam oscillation conditions. The width of the IML is calculated as the average width for the thickness of the Si-layer and

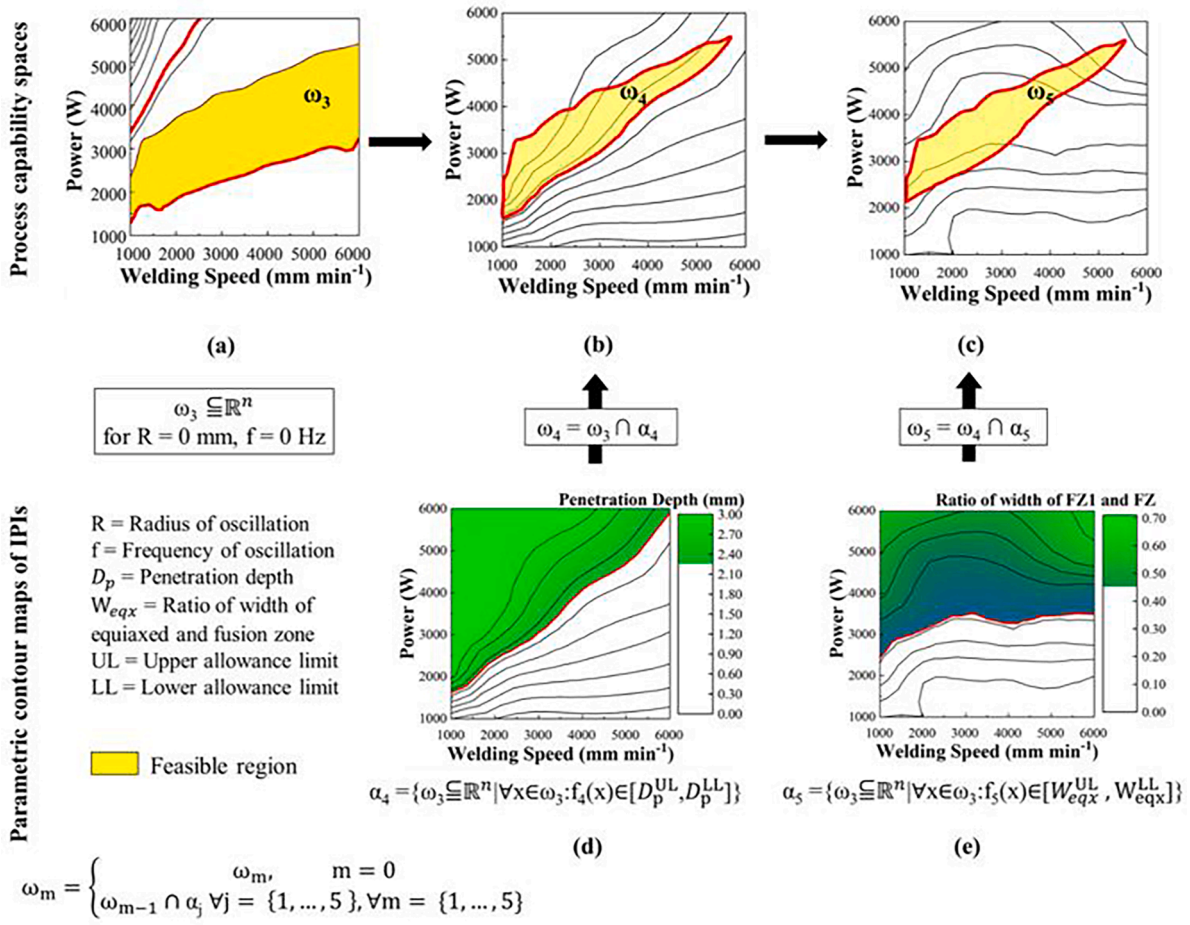

Fig. 6. Process capability space (C_p-Space) for no oscillation condition (where $R = 0$ mm and $f = 0$ Hz). The top row shows the process capability spaces (at each step with an intersection with IPIs) and the bottom row shows the parametric contour maps of each IPIs with the allowance limit. Image has been reproduced and modified from (Gäumann et al., 2001) with permission.

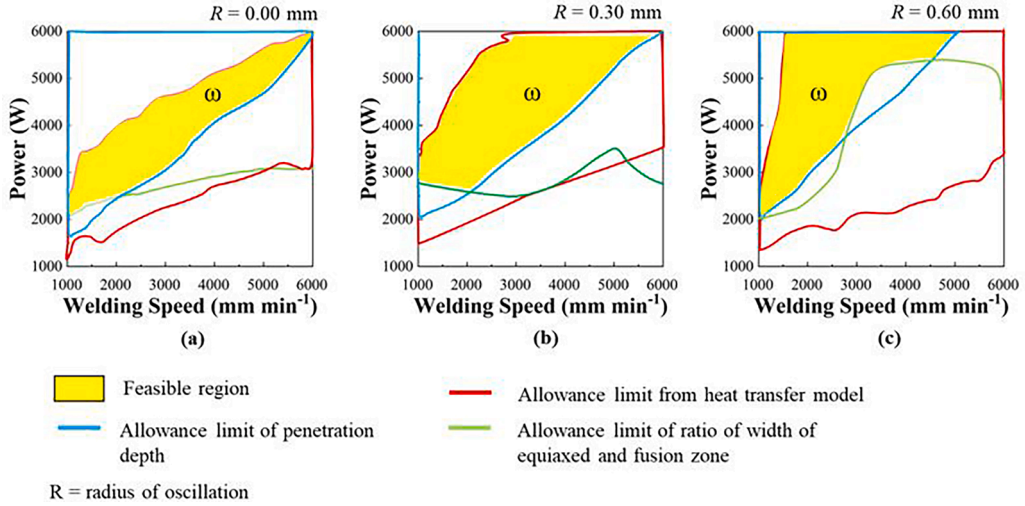

Fig. 7. shows the process capability space for three process parameters to show the 3D response surface as a stacked-up 2D contour map. The z-axis for the 3D response surface is the radius of oscillation (R) which is varied at (a) $R = 0$ mm, (b) $R = 0.30$ mm and (c) $R = 0.60$ mm.

Mg-layer in and around the fusion zone. The movement of alloying elements is governed by both diffusion (due to thermal and concentration gradients) and convection (due to fluid flow in the molten weld pool) which is dependent on the process parameters. At a constant laser power, this ratio increases with an increase in welding speed up to critical welding speed and then again decreases with a further increase in welding speed. At a constant welding speed, the ratio of the width of the intermixing layer (IML) and the width of the fusion zone decreases which suggests that the intermixing is more dominant towards the conduction mode of welding and this type of movement is more

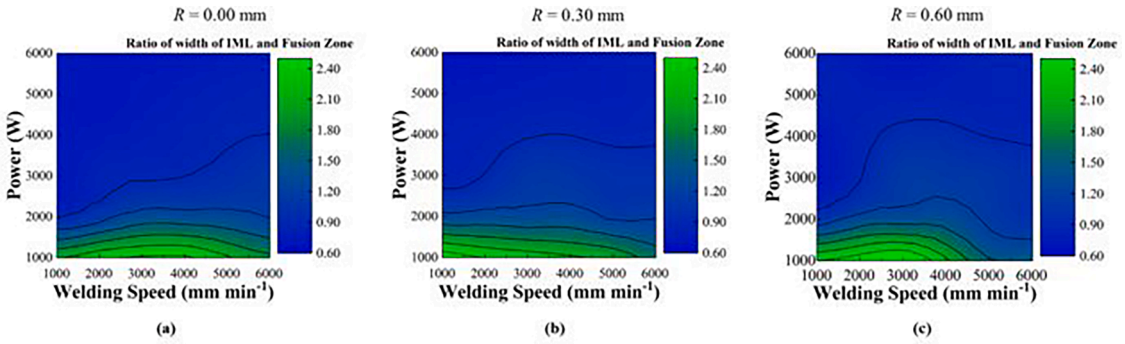

Fig. 8. Parametric contour maps for laser power vs welding speed with and without oscillation conditions at a constant frequency of oscillation of 200 Hz. (a-c) shows a contour map for the ratio of the width of intermixing layer and the width of the fusion zone.

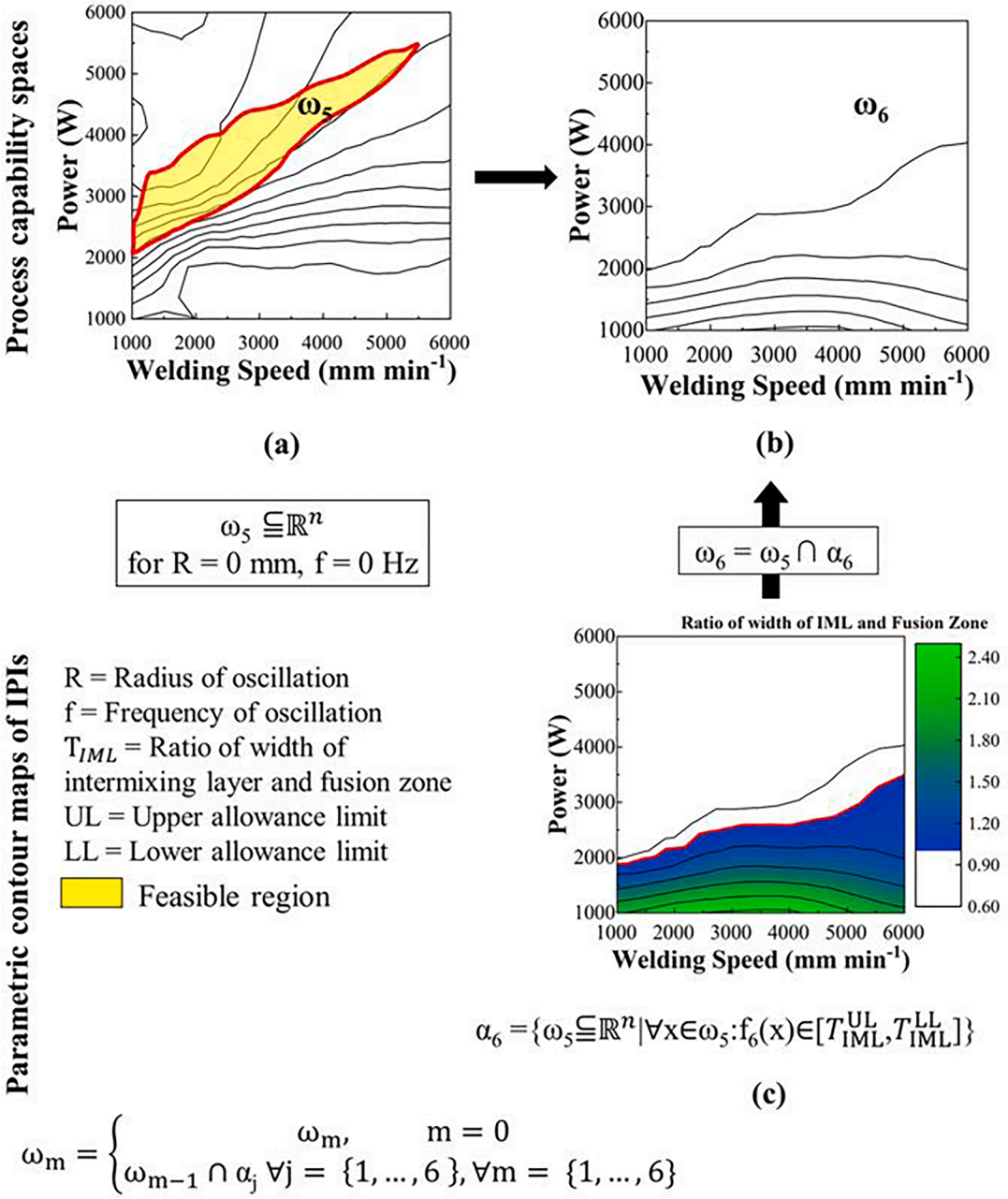

Fig. 9. Process capability space (C_p-Space) for no oscillation condition (where $R = 0$ mm and $f = 0$ Hz). The top row shows the process capability spaces (at each step with an intersection with IPIs) and the bottom row shows the parametric contour maps of each IPIs with the allowance limit.

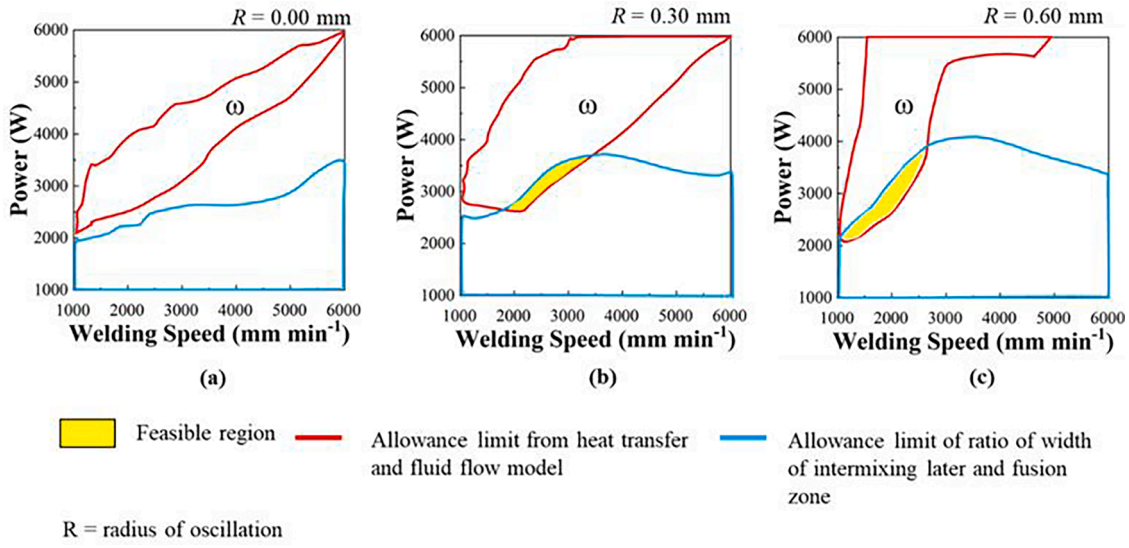

Fig. 10. shows the final process capability space for three process parameters to show the 3D response surface as a stacked-up 2D contour map. The z-axis for the 3D response surface is radius of oscillation which is varied at (a) $R = 0$ mm, (b) $R = 0.30$ mm and (c) $R = 0.60$ mm.

dominant due to diffusion phenomena. Also, the width of the intermixing layer is more as compared to the no oscillation condition. This is due to the churning action by the oscillating beam leading to more convection in the molten pool.

Fig. 9 shows the process capability space for no oscillation welding based on the ratio of the width of IML and fusion zone. The ω_5 is the process capability space from the combined heat transfer and fluid flow model which acts as a parameters space for the mass transport model combined with previous models. The lower limit of the ratio of the width of intermixing later and fusion zone is taken as 1 as in principle the modification of chemical composition should be at least cover the whole fusion zone. From Fig. 9, it is clear there is no solution due to the two opposing boundary constraints. As in this section, the intermixing is more prevalent close to the conduction mode of welding while the requirement from the section is to have higher penetration which leads to no solution. This shows that the material will be prone to cracking and is independent of the process parameters. To overcome the problem there should be a balance between the depth of penetration and material mixing. Less mixing at a high depth of penetration makes the joint susceptible to cracking which leads to failure and at a low depth of penetration joint will have lower mechanical strength due to lower coalescence between the plates. It also suggests that there is a need to modify the linear welding in the RLW process in such a way that it increases the mixing at a higher depth of penetration such as beam oscillation. Other way is to modify the chemical composition of the weld either by adding the alloying element in the base metal which increase the grain refinement such as Titanium or using filler wire.

Fig. 10 shows the effect of beam oscillation on the final process capability space. The results show that with the application of beam oscillation small intersecting region is there which increases with an increase in oscillation radius. The increase in the feasible region is due to the increase in convection due to the churning action of the beam oscillation.

Conclusions

This research work aimed to develop a framework for the quick selection of robust welding process parameters during the early design phase to achieve the weld quality requirements and to comprehensively understand the effect of different laser welding process parameters on the weld thermal cycle, fluid flow, solidification behaviour, grain morphology and mass transport during the laser butt-welding of high-strength aluminium alloys with consideration to beam oscillation. This was accomplished by developing the Multiphysics numerical model to simulate heat transfer, fluid flow and mass transport for laser welding and including key laser welding technological advancements such as beam oscillation as input parameters in the numerical model. The key conclusions are:

- The process capability space refining strategy presented, decreases the number of paths within the process capability space from the initial parameter settings to optimise process parameters.
- The area of process capability space increases with the application of beam oscillation. This increase in area exhibits the increase in flexibilities due to the application of beam oscillation, as the process will be more robust due to larger acceptable regions and smaller fall-out areas.
- The final process capability space shows that the oscillation condition has no solution while the beam oscillation condition generates the solution. This indicates that the chemical composition of the fusion zone is far away from the peak of crack susceptibility and can be attained during the beam oscillation condition. The final process capability space increases with an increase in the radius of oscillation.

Determining process parameters for cobotic or manual repair in laser welding demands a comprehensive approach that extends beyond the parameters employed in robotic welding during production. Factors such as material condition, defect analysis, accessibility, operator skill, real-time monitoring, safety considerations, environmental factors, and quality assurance requirements must be carefully considered to ensure consistent and high-quality repair outcomes. By integrating these insights into parameter selection, manufacturers can effectively address repair challenges and achieve the goal of zero-defect manufacturing in laser welding applications.

CRediT authorship contribution statement

Anand Mohan: Writing – review & editing, Writing – original draft, Visualization, Validation, Software, Methodology, Investigation, Funding acquisition, Formal analysis, Data curation, Conceptualization. **Qamar Hayat:** Writing – review & editing, Conceptualization. **Soumitra Kumar Dinda:** Writing – review & editing, Visualization, Conceptualization. **Venkat Vivek Pamarthi:** Conceptualization. **Pasquale**

Franciosa: Validation, Supervision. **Dariusz Ceglarek:** Supervision, Project administration, Methodology, Funding acquisition, Conceptualization. **Michael Auinger:** Writing – review & editing, Supervision, Resources, Project administration, Methodology, Funding acquisition, Conceptualization.

Declaration of competing interest

The authors declare that they have no known competing financial interests or personal relationships that could have appeared to influence the work reported in this paper.

Data availability

Data will be made available on request.

Acknowledgement

This study was financially supported by EPSRC MSI (Research Centre for Smart, Collaborative Industrial Robots) (Grant No. EP/V062158/1).

References

Davies, G., 2003. Materials for Automobile Bodies. Mater. Automobile Bodies 1–277. https://doi.org/10.1016/B978-0-7506-5692-4.X5014-6.

Goede, M., Stehlin, M., Rafflenbeul, L., Kopp, G., Beeh, E., 2009. Super Light Car-lightweight construction thanks to a multi-material design and function integration. Eur. Transport Res. Rev. 1, 5–10.

Sánchez Amaya, J.M., Amaya-Vázquez, M.R., Botana, F.J, 2013. Laser Welding of Light Metal alloys: Aluminium and Titanium alloys. Handbook of Laser Welding Technologies. Elsevier Inc., pp. 215–254, 10.1533/9780857098771.2.215.

Ramiarison, H., Barka, N., Mirakhorli, F., Nadeau, F., Pilcher, C., 2022. Parameter optimization for laser welding of dissimilar aluminum alloy: 5052-H32 and 6061-T6 considering wobbling technique. Int. J. Adv. Manuf. Technol. 118, 4195–4211. https://doi.org/10.1007/s00170-021-08122-y.

Ceglarek, D., Colledani, M., Váncza, J., Kim, D.Y., Marine, C., Kogel-Hollacher, M., 2015. Rapid deployment of remote laser welding processes in automotive assembly systems. CIRP Annals 64, 389–394. https://doi.org/10.1016/J.CIRP.2015.04.119.

Hagenlocher, C., Sommer, M., Fetzer, F., Weber, R., Graf, T., 2018. Optimization of the solidification conditions by means of beam oscillation during laser beam welding of aluminum. Mater. Des. 160, 1178–1185. https://doi.org/10.1016/j.matdes.2018.11.009.

Hagenlocher, C., Weller, D., Weber, R., Graf, T., 2019. Reduction of the hot cracking susceptibility of laser beam welds in AlMgSi alloys by increasing the number of grain boundaries. Sci. Technol. Welding Joining 24, 313–319.

Ozkat, E.C., Franciosa, P., Ceglarek, D., 2017a. Development of decoupled multi-physics simulation for laser lap welding considering part-to-part gap. J. Laser Appl. 29, 022423.

Mahamood, R.M., Akinlabi, E.T., 2018. Advanced Noncontact Cutting and Joining Technologies: Micro- and Nano-Manufacturing, 1st ed. Springer, Cham.

Salminen, A., Piili, H., Purtonen, T., 2010. The characteristics of high power fibre laser welding. J. Mech. Eng. Sci. 224, 1019–1029.

Quintino, L., Costa, A., Miranda, R., Yapp, D., Kumar, V., Kong, C.J., 2007. Welding with high power fiber lasers – A preliminary study. Mater. Des. 28, 1231–1237. https://doi.org/10.1016/J.MATDES.2006.01.009.

Guan, Q., Long, J., Yu, P., Jiang, S., Huang, W., Zhou, J., 2019. Effect of steel to aluminum laser welding parameters on mechanical properties of weld beads. Opt. Laser. Technol. 111, 387–394. https://doi.org/10.1016/j.optlastec.2018.09.060.

Chatterjee, S., Abinandanan, T.A., Chattopadhyay, K., 2006. Microstructure development during dissimilar welding: case of laser welding of Ti with Ni involving intermetallic phase formation. J. Mater. Sci. 41, 643–652. https://doi.org/10.1007/S10853-006-6480-4, 2006 41:3.

Zhang, L-J, Zhang, G.F., Bai, X.Y., Ning, J., Zhang, X.J., 2016. Effect of the process parameters on the three-dimensional shape of molten pool during full-penetration laser welding process. Int J Adv Manuf Technol 86, 1273–1286. https://doi.org/10.1007/s00170-015-8249-x.

Speka, M., Matteï, S., Pilloz, M., Ilie, M., 2008. The infrared thermography control of the laser welding of amorphous polymers. NDT E Int. 41, 178–183. https://doi.org/10.1016/J.NDTEINT.2007.10.005.

Moradi, M., Ghoreishi, M., 2011. Influences of laser welding parameters on the geometric profile of NI-base superalloy Rene 80 weld-bead. Int. J. Adv. Manuf. Technol. 55, 205–215. https://doi.org/10.1007/S00170-010-3036-1.

Gao, Z., Shao, X., Jiang, P., Cao, L., Zhou, Q., Yue, C., 2016. Parameters optimization of hybrid fiber laser-arc butt welding on 316L stainless steel using Kriging model and GA. Opt. Laser. Technol. 83, 153–162. https://doi.org/10.1016/J.OPTLASTEC.2016.04.001.

Courtois, M., Carin, M., Le Masson, P., Gaied, S., Balabane, M, 2016. Guidelines in the experimental validation of a 3D heat and fluid flow model of keyhole laser welding. J. Phys. D. Appl. Phys. 49 https://doi.org/10.1088/0022-3727/49/15/155503.

Pang, S., Chen, L., Zhou, J., Yin, Y., Chen, T., 2011. A three-dimensional sharp interface model for self-consistent keyhole and weld pool dynamics in deep penetration laser welding. J. Phys. D. Appl. Phys. 44 https://doi.org/10.1088/0022-3727/44/2/025301.

Rai, R., Elmer, J.W., Palmer, T.A., Debroy, T., 2007. Heat transfer and fluid flow during keyhole mode laser welding of tantalum, Ti-6Al-4V, 304L stainless steel and vanadium. J. Phys. D: Appl. Phys. 40, 5753–5766. https://doi.org/10.1088/0022-3727/40/18/037.

Otto A., Koch H., Leitz K., Schmidt M. Numerical simulations - a versatile approach for better understanding dynamics in laser material processing 2011;12:11–20. https://doi.org/10.1016/j.phpro.2011.03.003.

Chen, Z., Gao, X., 2014. Detection of weld pool width using infrared imaging during high-power fiber laser welding of type 304 austenitic stainless steel. Int J Adv Manuf Technol 74, 1247–1254. https://doi.org/10.1007/s00170-014-6081-3.

Chen, L., Wang, C., Mi, G., Zhang, X., 2021. Effects of laser oscillating frequency on energy distribution, molten pool morphology and grain structure of AA6061/AA5182 aluminum alloys lap welding. J. Mater. Res. Technol. 15, 3133–3148. https://doi.org/10.1016/J.JMRT.2021.09.141.

Lankalapalli, K.N., Tu, J.F., Gartner, M., 1996. A model for estimating penetration depth of laser welding processes. J. Phys. D. Appl. Phys. 29, 1831. https://doi.org/10.1088/0022-3727/29/7/018.

Ion, J.C., Shercliff, H.R., Ashby, M.F., 1992. Diagrams for laser materials processing. Acta Metallurgica et Materialia 40, 1539–1551. https://doi.org/10.1016/0956-7151(92)90097-X.

Norouzian, M., Amne Elahi, M., Plapper, P, 2023. A review: suppression of the solidification cracks in the laser welding process by controlling the grain structure and chemical compositions. J. Adv. Joining Processes 7. https://doi.org/10.1016/j.jajp.2023.100139.

Mukherjee, T., Manvatkar, V., De, A., DebRoy, T., 2017. Dimensionless numbers in additive manufacturing. J. Appl. Phys. 121 https://doi.org/10.1063/1.4976006.

Mannik, L., Brown, S.K., 1990. A relationship between laser power, penetration depth and welding speed in the laser welding of steels. J. Laser Appl. 2, 22–25. https://doi.org/10.2351/1.4745264.

Leong, K.H., Geyer, H.K., Sabo, K.R., Sanders, P.G., 1997. Threshold laser beam irradiances for melting and welding. J. Laser Appl. 9, 227–231. https://doi.org/10.2351/1.4745464.

Franciosa, P., Gerbino, S., Ceglarek, D., 2016. Fixture capability optimisation for early-stage design of assembly system with compliant parts using nested polynomial chaos expansion. Procedia CIRP. 41, 87–92. https://doi.org/10.1016/j.procir.2015.12.101.

Mannar, K., Ceglarek, D., 2010. Functional capability space and optimum process adjustments for manufacturing processes with in-specs failure. IIE Trans. (Inst. Indust. Eng.) 42, 95–106. https://doi.org/10.1080/07408170902789027.

Ozkat, E.C., Franciosa, P., Ceglarek, D., 2017b. Laser dimpling process parameters selection and optimization using surrogate-driven process capability space. Opt. Laser. Technol. 93, 149–164.

Coniglio, N., Cross, C.E., Michael, T., Lammers, M., 2008. Defining a critical weld dilution to avoid solidification cracking in aluminum. Weld. J. 87, 237–247.

Weller, D., Hagenlocher, C., Steeb, T., Weber, R., Graf, T., 2018. Self-restraint hot cracking test for aluminum alloys using digital image correlation. Procedia CIRP. 74, 430–433. https://doi.org/10.1016/J.PROCIR.2018.08.165.

BJ, C., 1960. Generalized theory of supersolidus cracking in welds and castings. Br. Weld J. 7, 508–512.

Bamberg, P., Schiebahn, A., Marzzona, A., Christ, M., Reisgen, U., 2024. Optimization of weldability and joint strength of Al-Mg-Si with additional Al-Si cladding based on a design of experiments investigation. J. Adv. Joining Processes 9. https://doi.org/10.1016/J.JAJP.2024.100206.

Troise, M., Krichel, T., Olschok, S., Reisgen, U., 2024. Investigation of the influence of pulse parameters on the resulting weld seam quality in pulsed electron beam welding of AW 6061. J. Adv. Joining Processes 9. https://doi.org/10.1016/j.jajp.2023.100183.

Goyal, R., El-zein, M., 2020. Influence of laser weld shape on mechanical and fatigue behaviour of single lap laser welded joints. J. Adv. Joining Processes 1. https://doi.org/10.1016/j.jajp.2020.100018.

Chen, L., Wang, C., Xiong, L., Zhang, X., Mi, G., 2020. Microstructural, porosity and mechanical properties of lap joint laser welding for 5182 and 6061 dissimilar aluminum alloys under different place configurations. Mater. Des. 191, 108625 https://doi.org/10.1016/J.MATDES.2020.108625.

Dinda, SK, Das, D, Mohan, A, Srirangam, P, Roy, GG, 2021. Effect of Beam Oscillation on Electron Beam Butt Welded Dual-Phase (DP600) Steel to 5754 Aluminum Alloy Joints. Metall Mater Trans A Phys Metall Mater Sci 52, 1723–1731. https://doi.org/10.1007/s11661-021-06181-0.

Easton, M.A., Wang, H., Grandfield, J., Davidson, C.J., Stjohn, D.H., Sweet, L.D., et al., 2012. Observation and prediction of the hot tear susceptibility of ternary Al-Si-Mg Alloys. Metallurgical and Materials Transactions A. https://doi.org/10.1007/s11661-012-1132-6.

Farrokhi, F., Endelt, B., Kristiansen, M., 2019. A numerical model for full and partial penetration hybrid laser welding of thick-section steels. Opt. Laser. Technol. 111, 671–686. https://doi.org/10.1016/J.OPTLASTEC.2018.08.059.

Atabaki, M.M., Nikodinovski, M., Chenier, P., Ma, J., Liu, W., Kovacevic, R., 2014. Experimental and numerical investigations of hybrid laser arc welding of aluminum alloys in the thick T-joint configuration. Opt. Laser. Technol. 59, 68–92.

Geng, S., Jiang, P., Shao, X., Guo, L., Gao, X., 2020. Heat transfer and fluid flow and their effects on the solidification microstructure in full-penetration laser welding of aluminum sheet. J. Mater. Sci. Technol. 46, 50–63. https://doi.org/10.1016/j.jmst.2019.10.027.

Wu, J., Zhang, H., Feng, Y., Luo, B.B., 2018. 3D multiphysical modelling of fluid dynamics and mass transfer in laser welding of dissimilar materials. Metals. (Basel) 8. https://doi.org/10.3390/met8060443.

Mohan, A., Franciosa, P., Ceglarek, D., Auinger, M., 2023a. Numerical simulation of transport phenomena and its effect on the weld profile and solute distribution during laser welding of dissimilar aluminium alloys with and without beam oscillation. Int. J. Adv. Manuf. Technol. 124, 3311–3325. https://doi.org/10.1007/s00170-022-10623-3.

Abderrazak, K., Bannour, S., Mhiri, H., Lepalec, G., Autric, M., 2009. Numerical and experimental study of molten pool formation during continuous laser welding of AZ91 magnesium alloy. Comput. Mater. Sci. 44, 858–866.

Slováček, M., Diviš, V., Junek, L., Ochodek, V., 2005. Numerical simulation of the welding process — distortion and residual stress prediction, heat source model determination. Welding World 49, 15–29.

Sun, T., Mohan, A., Liu, C., Franciosa, P., Ceglarek, D., 2022. The impact of Adjustable-Ring-Mode (ARM) laser beam on the microstructure and mechanical performance in remote laser welding of high strength aluminium alloys. J. Mater. Res. Technol. 21, 2247–2261. https://doi.org/10.1016/J.JMRT.2022.10.055.

Mohan, A., Ceglarek, D., Franciosa, P., Auinger, M., 2023b. Numerical study of beam oscillation and its effect on the solidification parameters and grain morphology in remote laser welding of high-strength aluminium alloys. Sci. Technol. Welding Joining. https://doi.org/10.1080/13621718.2022.2163341.

Shi, Q., Gu, D., Xia, M., Cao, S., Rong, T., 2016. Effects of laser processing parameters on thermal behavior and melting/solidification mechanism during selective laser melting of TiC/Inconel 718 composites. Opt. Laser. Technol. 84, 9–22.

Behúlová, M., Babalová, E., Sahul, M., 2017. Design of laser welding parameters for joining Ti Grade 2 and AW 5754 aluminium alloys using numerical simulation. Adv. Mater. Sci. Eng. 2017, 1–15.

Guo, H., Hu, J., Tsai, H.L., 2010. Three-dimensional modeling of gas metal arc welding of aluminum alloys. J. Manuf. Sci. Eng. 132, 1–10.

Swift- D.T., Gick A.E.F. 1973. Analytical study indicates that present laser beam weld-ing capabilities may be extended tenfold. Penetration Welding with Lasers.

COMSOL. Using the Material Libraries in COMSOL Multiphysics® | COMSOL Blog 2020. https://www.comsol.com/blogs/using-the-material-libraries-in-comsol-multiphysics/(accessed August 16, 2022).

Mohan, A., Ceglarek, D., Auinger, M., 2022a. Numerical modelling of thermal quantities for improving remote laser welding process capability space with consideration to beam oscillation. Int. J. Adv. Manuf. Technol. 123, 761–782. https://doi.org/10.1007/s00170-022-10182-7.

Mohan, A., Ceglarek, D., Auinger, M., 2022b. Effect of beam oscillation on the fluid flow during laser welding. Mater. Today Proc. 59, 1846–1851. https://doi.org/10.1016/j.matpr.2022.04.435.

Hunt, J.D., 1984. Steady state columnar and equiaxed growth of dendrites and eutectic. Mater. Sci. Eng. 65, 75–83. https://doi.org/10.1016/0025-5416(84)90201-5.

Gäumann, M., Bezençon, C., Canalis, P., Kurz, W., 2001. Single-crystal laser deposition of superalloys: processing–microstructure maps. Acta Mater. 49, 1051–1062. https://doi.org/10.1016/S1359-6454(00)00367-0.

Flood, S.C., Hunt, J.D., 1987. Columnar and equiaxed growth: II. Equiaxed growth ahead of a columnar front. J. Cryst. Growth 82, 552–560. https://doi.org/10.1016/0022-0248(87)90347-2.

Vandyoussefi, M., Greer, A.L., 2002. Application of cellular automaton–finite element model to the grain refinement of directionally solidified Al–4.15 wt% Mg alloys. Acta Mater. 50, 1693–1705. https://doi.org/10.1016/S1359-6454(02)00015-0.